RESEARCH METHODS

Label-free structural and functional volumetric imaging by dual-modality optical-Raman projection tomography

Nan Wang[1,2], Xinyu Wang[1,2], Tianyu Yan[1,2], Hui Xie[1]*, Lin Wang[3], Feng Ren[1], Dan Chen[2], Dongjie Zhang[1], Qi Zeng[1], Shouping Zhu[2,4]*, Xueli Chen[1,2,4,5]*

Copyright © 2023 The Authors, some rights reserved; exclusive licensee American Association for the Advancement of Science. No claim to original U.S. Government Works. Distributed under a Creative Commons Attribution NonCommercial License 4.0 (CC BY-NC).

Mesoscale volumetric imaging is of great importance for the study of bio-organisms. Among others, optical projection tomography provides unprecedented structural details of specimens, but it requires fluorescence label for chemical targeting. Raman spectroscopic imaging is able to identify chemical components in a label-free manner but lacks microstructure. Here, we present a dual-modality optical-Raman projection tomography (ORPT) technology, which enables label-free three-dimensional imaging of microstructures and components of millimeter-sized samples with a micron-level spatial resolution on the same device. We validate the feasibility of our ORPT system using images of polystyrene beads in a volume, followed by detecting biomolecules of zebrafish and *Arabidopsis*, demonstrating that fused three-dimensional images of the microstructure and molecular components of bio-samples could be achieved. Last, we observe the fat body of *Drosophila melanogaster* at different developmental stages. Our proposed technology enables bimodal label-free volumetric imaging of the structure and function of biomolecules in a large sample.

INTRODUCTION

Volumetric imaging technology has been increasingly used in biological research and applications, including cell metabolism, brain function, and developmental biology (*1*–*4*). It provides quantitative, three-dimensional (3D) and high-resolution image analysis of the whole sample. The volumetric images of a sample can be determined with a high resolution using optical sectioning and light-sheet microscopy. Optical sectioning can obtain the image of specimen stacks by neglecting the out-of-focus laser area in each image plane, which is highly discrepant and permits 3D reconstructions (*5*, *6*). However, this technique suffers from the limitations of being time-consuming for a volume of hundreds of micrometers (*7*) and that it may not record fast biological events or light-sensitive samples. To overcome the time-consumption drawback, light-sheet microscopy was introduced. In this system, the illumination beam should first be transformed into a sheet to scan the focal plane images of samples. Then, the detection system should be perpendicular to the laser to collect stacks of images from different layers of a sample for 3D reconstruction. Although this technology provides high-resolution and high-speed volumetric imaging of biological samples ranging from cells to embryos (*8*, *9*), the quality of the image degenerates as the distance between the objective lens and sample surface increases (*10*).

Optical projection tomography (OPT) is an emerging analytical tool to monitor the microstructure composition or biochemical information of biological specimens in a 3D volume, including proteins, cells, tissues, and organisms (*2*, *7*, *11*). With light transmission, OPT can improve the quality of an image by rotating the sample (*12*) and collecting the projection images from different angles; thus, 3D structural information of samples can be reconstructed (*11*, *13*, *14*). However, this method lacks chemical contrast. Combined with labeling methods, all interesting internal structures or the complex genetic activities of a biomedical specimen can be simultaneously emphasized. Nevertheless, fluorescence label technique may terminate the normal life process or stimulate other side effects, perturbing the living organism (*12*, *15*). Besides, label methods cannot do repeated measurements of the same samples over extended periods of time and may lead to an increased probability of errors originating from variations in specimens (*16*). Although many newly developed labeling techniques have been reported for promising applications, label-free imaging is still highly desired for investigating biological specimens.

Label-free imaging techniques, such as second harmonic generation (SHG), third harmonic generation (THG), infrared microscopy (IR), confocal reflection (CR), and optical coherence tomography (OCT), have been proposed to characterize the 3D specific biochemical composition and molecular structure (*17*–*22*). Although the chemical composition and topography of a system can be determined using IR microscopy, it suffers from the interference of water absorption. Besides, its spatial resolution is substandard (*22*). Meanwhile, THG, CR, and OCT can reveal the morphological features of a specimen, but they lack the chemical contrast for volumetric imaging (*17*, *20*, *21*). SHG imaging is primarily used to characterize collagen species, but the signal may be weak or absent (*17*–*19*). Raman imaging is another label-free imaging approach, which can provide quantitative and qualitative biochemical information as well as morphological information (*23*). Over the

[1]Biomedical Photonics and Molecular Imaging Laboratory, School of Life Science and Technology, Xidian University, and Xi'an Key Laboratory of Intelligent Sensing and Regulation of Trans-Scale Life Information, Xi'an, Shaanxi 710126, China. [2]Engineering Research Center of Molecular and Neuro Imaging, Ministry of Education, Xi'an, Shaanxi 710126, China. [3]School of Computer Science and Engineering, Xi'an University of Technology, Xi'an, Shaanxi 710048, China. [4]International Joint Research Center for Advanced Medical Imaging and Intelligent Diagnosis and Treatment, School of Life Science and Technology, Xidian University, Xi'an, Shaanxi 710126, China. [5]Innovation Center for Advanced Medical Imaging and Intelligent Medicine, Guangzhou Institute of Technology, Xidian University, Guangzhou, Guangdong 51055, China.
*Corresponding author. Email: xlchen@xidian.edu.cn (X.C.); spzhu@xidian.edu.cn (S.Z.); hxie@xidian.edu.cn (H.X.)

past decade, Raman imaging has been a leading modality for noninvasive and in vivo imaging of biological applications, providing a unique "molecular fingerprint." Coherent Raman scattering microscopy–based sectioning can map the chemical composition of a specimen in volumes (*17*, *24*). However, it is heavily time-consuming when the sample is several hundred microns or more across. Light-sheet Raman microscopy can examine the chemical composition in a volume, but it interferes with the background of autofluorescence (*25*). In a previous work, combined with projection strategy, we proposed Bessel beam–based stimulated Raman projection microscopy and tomography for high-speed volumetric chemical imaging (*26*). However, because of the nonlinear effect of the excitation lasers, this technique has a small field of view and lacks the structural information. Wide-field Raman imaging plays an important role in probing the molecular distribution of large field-of-view samples while achieving a high resolution. Combined with the projection concept, it facilitates the 3D high-resolution imaging of large-scale samples. However, such a technique cannot visualize the specific spatial distribution of the sample microstructure.

In this work, we present a dual-modality optical-Raman projection tomography (ORPT) for label-free structural and molecular volumetric imaging (*27*) based on the concept that the fusion image can be obtained from the Raman projection tomography and OPT. The ORPT technique can obtain the optical and Raman projection images with micron-level spatial resolution and millimolar sensitivity, respectively, by rotating a sample and collecting the projection images from different angles. Thus, the chemical composition and microstructural information of a sample can be mapped in a 3D volume. First, we investigated the relationship between the laser power, sample concentration, and intensity of the Raman signal. We performed an experimental analysis of the system, which showed a good agreement with the theory. Then, we validated the feasibility of the ORPT system and the performance of the reconstruction algorithm by imaging single and multiple polystyrene (PS) beads, respectively. Furthermore, we examined the capability of the ORPT system for imaging the microstructure and chemical components of biological species, such as zebrafish and *Arabidopsis thaliana*. Last, we explored the potential of our system in detecting the fat body of *Drosophila melanogaster* at different developmental stages. Comparative analysis of our findings showed that our ORPT system has superior capability in detecting the microstructural information. Besides, it can be further developed to visualize the molecular distribution and dynamic process of samples in a 3D volume.

RESULTS

The ORPT system

A schematic overview of our ORPT system is depicted in Fig. 1A, where we obtained dual-modality projection images of the samples from two beams. We used the first laser beam as a Raman signal excitation source, which operated at 532-nm laser [MSL-FN-532, Changchun New Industries Optoelectronics Tech. Co., Ltd. (CNI), China)] with 300 mW and narrow linewidth (<0.00001 nm) and had a good monochromaticity. To adjust the power of the laser, we first passed it from a circular variable attenuator (OD0-OD3, CNI, China) and then expanded and collimated it by a 4f system, followed by irradiation of the sample. We housed a filter wheel (CFW6/M, Thorlabs, USA) with different center wavelength filters and an edge filter in a lens tube for the purification of the generated Raman projection images, obtained by a charge-coupled device (CCD; iKon-M 934, Andor, USA). To magnify the captured projection images between ×1.4 and ×9, we mounted a lens (Zoom 6000, Navitar, USA) on the CCD. The second beam was a faced light source [BT-50*50SW, Oriental System Engineering (OSE), Singapore] and worked as a reference light beam to help the Raman channels to focus the samples on the focal plane before imaging. This second beam also provided diffuse reflection light with adjustable intensity for microstructural information of a sample in a 3D volume. Thus, we collected the projection images of this light path by the same detector. The sample holder is displayed in Supplementary Information 1.

Performance of the ORPT system

Spatial resolution and sensitivity are important factors that affect the performance of an imaging system. To estimate the spatial resolution of the ORPT system, we selected different images with a resolution test target (1951 USAF, Thorlabs, USA) in different magnifications, obtained from the CCD. One of the images is shown in fig. S1A, where the magnification is ×9. We then extracted a profile across the line pairs of the image and calculated its shock response. When the shock response is fitted with a Gaussian curve as shown in Fig. 1B, then the spatial resolution is determined from the full width at half maximum of the fitted Gaussian curve. The value was found to be 5.12 μm when the magnification was ×9, while it was 36.42 μm when the magnification was ×1.4, as shown in Fig. 1C.

In the next stage, we evaluated the sensitivity of the ORPT system from the CH_2 symmetric stretching of dimethyl sulfoxide (DMSO), diluted in deuterium oxide (D_2O). At 141 mM concentration, the Raman signal of DMSO can be resolved with a signal-to-noise ratio (SNR) of 1.97, as shown in fig. S1B. Figure 1D depicts the Raman signal intensity as a function of the sample concentration, demonstrating an estimated detection limit of 70 mM DMSO. These results proved a millimolar sensitivity of our ORPT system in the Raman signal detection.

Furthermore, using DMSO as the test object, we also investigated the effect of the Raman signal on the concentration and the input laser powers, using DMSO as the test object. As shown in Fig. 1E, the results revealed that the Raman signal linearly decreased along with the decrease in the sample concentration [coefficient of determination (R^2) = 0.962]. Besides, the Raman signal was shown to be linearly dependent on the laser power (R^2 = 0.997), as shown in fig. S1C. Figure 1E presents the Raman images of DMSO as the laser power was reduced to 26.1 mW. In this case, the lower detecting intensity was responsible for the limited signal detection of the laser. These values were also consistent and showed a similar trend as predicted by theory (*28*). The characterization of Raman signal can be found in Supplementary Information 2. Figure 1F presents a workflow of the data acquisition and processing.

Dual-modality ORPT imaging of PS beads

We investigated the feasibility of our ORPT system in the detection of optical-Raman signals in 3D and the probability of the filtered back-projection (FBP) algorithm for 3D reconstruction. First, we imaged single PS beads (100 μm in diameter) in agarose gel immobilized in a cylindrical capillary. Movies S1 and S2 show the observed optical and Raman projection images of single PS beads

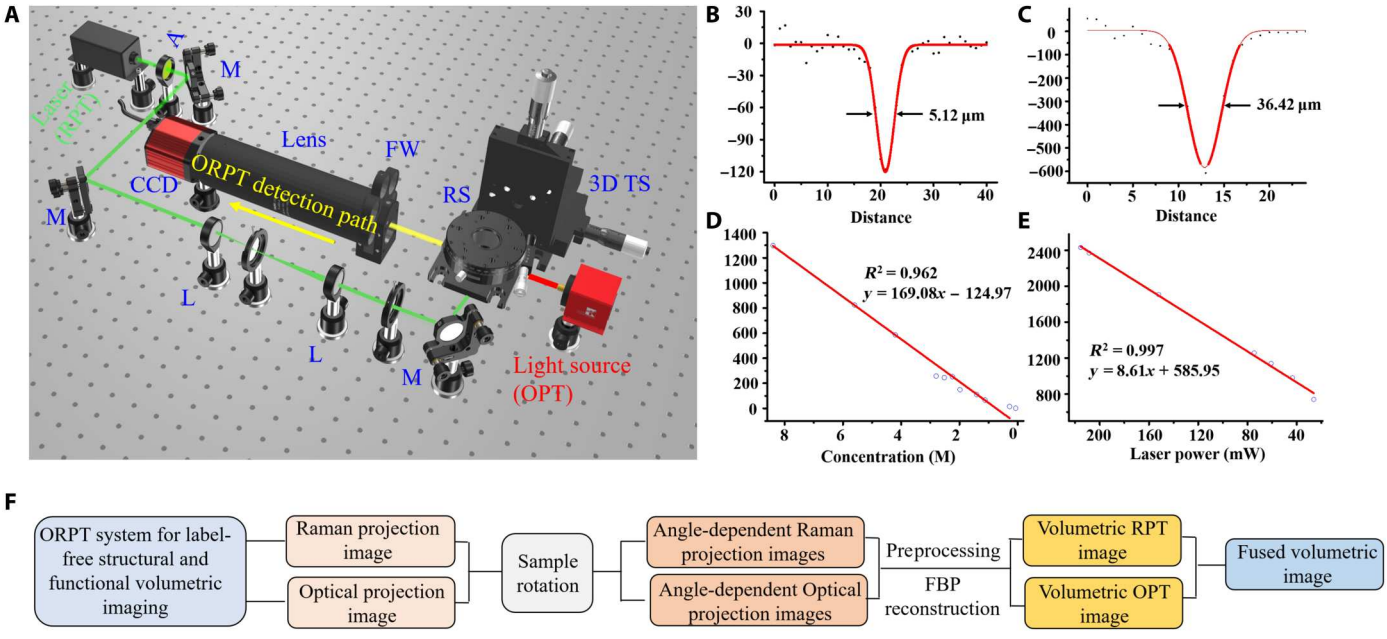

Fig. 1. The ORPT system. (**A**) Schematic figure of the ORPT system. A, attenuator; M, mirror; L, lens; RS, rotational stage; 3D TS, 3D translational stage; FW, filter wheel. (**B**) The fitting curve of the extracted profile is labeled in the resolution test target, indicating the optimal resolution of 5.12 μm. (**C**) The minimum spatial resolution of 36.42 μm. (**D**) Raman signal intensity as a function of the sample concentration. (**E**) The measured Raman signal from DMSO as a function of the laser power. (**F**) Workflow of data processing.

for 180 projections, respectively. We depicted the reconstructed 3D optical and Raman images in fig. S2 (A and D, respectively). Our findings showed that the reconstructed optical and Raman projection tomographic images of the beads could be well resolved, which were identical in terms of the location and morphology to the projection images (fig. S2, B and E). Furthermore, we fused the dual-modality tomographic reconstruction images (Fig. 2A) and verified them from the sectional images of the corresponding reconstructed volume along the transverse, coronal, and sagittal planes of the same beads, as shown in Fig. 2B. The flowchart of how to obtain a fused volumetric image from multiangle projection images is shown in fig. S3. The reconstructed fusion image in a 3D volume is presented in movie S3. These results strongly corroborate the dual-modality fusion image in morphology and localization and confirm that the structure and chemical composition of the beads can be well reconstructed with a little distortion. Furthermore, we imaged the multiple PS beads of 100 μm in a volume of ~1.48 mm by 1.48 mm by 1.48 mm using our ORPT system, and the results are shown in Fig. 2C. The related details are shown in movies S4 and S5 and fig. S2.

ORPT imaging of zebrafish

Zebrafish is an important model organism that is rapid, small, and easy to breed with a high optical transparency, which can provide direct visual access to biological processes (*29*, *30*). Moreover, zebrafish has about 81% of the genes associated with human diseases. Therefore, it has been established as a cancer model for the investigation of cancer cells and their microenvironment in preclinical cancer research, such as liver, leukemia, neuroblastoma, melanoma, pancreatic, and testicular cancer (*30*, *31*). Lipids and proteins are essential components of the metabolism during the development of zebrafish, and their distribution is strictly regulated to ensure proper activity and function of the organism (*30*). Thus, the image of related components in a living system is of great interest. The notochord is a reinforced axonal rod-like organ, which distinguishes chordates, like zebrafish, from other animals and plays a critical role in pattern formation (*32*–*34*). During development, the central cells of the zebrafish notochord form large vesicles, which eventually lead to tissue degeneration and form a vertebral column after the embryo period (*32*). The vacuolar cells and protein-rich fibrous muscle cells are generated as Raman images at 2950, 2845, and 1650 cm^{-1}, coming from both protein and lipid.

In this work, we imaged the zebrafish in the range of 2457 to 3123 cm^{-1} vibrational window and validated the usefulness of our ORPT system in imaging tissue biomolecules. First, we acquired optical image stacks of 180 projections by rotating the sample, as shown in movie S7 and fig. S4A. The reconstructed OPT image by the FBP algorithm can be found in fig. S4C. We observed that the structure of the zebrafish could be well resolved in a volume of ~4.43 mm by 4.43 mm by 4.43 mm, especially the large vesicles and protein-rich fibrous muscle. Next, we collected the Raman projection images (fig. S4B) at 1° per step, by rotating the sample for 3D reconstruction. We set the integral time to 8 s for each image. Movie S8 shows the projection images of 180 steps. The results of the Raman projection images (fig. S4B) and 3D reconstruction Raman image (fig. S4D) showed an obvious Raman signal in the large vesicles and vertebral column of zebrafish, representing the CH_3 stretching of protein in 2950 cm^{-1} and C-H stretching of lipid from CH_2 at 2850 cm^{-1}. Similarly, we also observed the Raman-like signal around the eyes. To qualitatively verify the origin of this signal, we tuned the filter wheel at different wave numbers to detect the suspicious signal. Unexpectedly, the signal

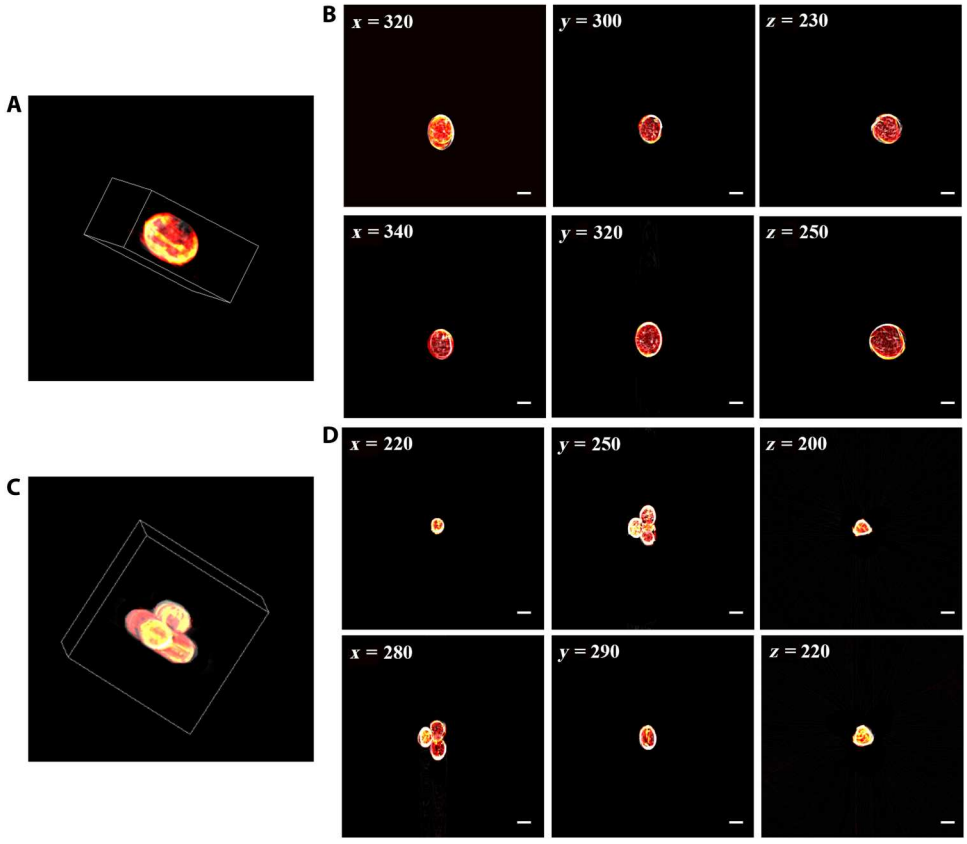

Fig. 2. Dual-modality fusion images of PS beads. (**A**) The fusion image of single PS beads of 100 μm in a volume of ~1.48 mm by 1.48 mm by 1.48 mm. (**B**) Sectional images of the single PS beads volume, acquired by the ORPT system at different views. (**C**) The volumetric fusion image of multiple PS beads (diameter in 100 μm). (**D**) Selected image slices of multiple PS beads along the sagittal, coronal, and transverse views, respectively. Scale bars, 100 μm.

intensity showed large differences at different wave numbers, in consistence with the corresponding Raman signal as reported elsewhere (see fig. S5) (*35*). The reconstructed 3D fusion image of zebrafish in the structure and chemical distribution is shown in Fig. 3A and movie S9. The fusion results revealed that the detected lipid or protein agreed well with the location of the corresponding structure. The selected slices in different views (coronal, sagittal, and transverse) displayed the fused structure where lipid or protein distributions are shown in Fig. 3B. Compared with the tomographic results, we found differences in the fine structures with little distortion, which was possibly due to discrepancies in the image depths, spatial resolution of the system, and other factors. These results confirmed the applicability of our ORPT system for in vivo imaging of biomolecules from the structure and molecule in a 3D volume.

ORPT imaging of *A. thaliana* stem

With its simple genetic transformation, cultivation protocols and a large number of genetic resources, the plant *A. thaliana* represents an excellent model organism for probing the plant cell wall. Its small genome size (the first sequenced plant genome) and fast generation time are responsible for the rapid characterization of treatment and mutations, playing a vital role in plant genetics and biology (*36*, *37*). *Arabidopsis* has been extensively used for the investigation of proteomics and gene knockouts and the study of the plant polymers, including cellulose, lignin, wax, and hemicellulose (*38*–*42*). Thus, the application of imaging analysis tools in *Arabidopsis* is crucial and desirable.

Here, we demonstrated the C-H and CH_2 stretching bonds of transparent *Arabidopsis* stem with our ORPT system in the 2457 to 3123 cm^{-1} vibrational window, representing the spatial distribution of the measured cell walls and related lipid components. The 3D structural and molecular reconstruction image of the stem in a volume of ~1.48 mm by 1.48 mm by 1.48 mm is shown in Fig. 4A. The sectional images along different planes, as selected from the reconstructed volume, are shown in Fig. 4B, which shows the structure of the pericycle and the epidermis of the stem, while the Raman signal can be observed around the pericycle, which is also consistent with the already reported data (*36*). However, we observed a slight positional mismatch between the distribution of lipid in the stem and the corresponding structure information along the coronal and sagittal planes. This might be due to the bias of the sample rotation during data acquisition of the different modalities. Besides, the Raman signal of the transparent stem is weak and small, which makes it difficult to visualize it. However, this can be optimized in the subsequent experiment. These results proved the capability of our system in detecting plants, which may ultimately help to understand the molecular biology of many plant traits. The related dual-modality projection movies, projection images, and

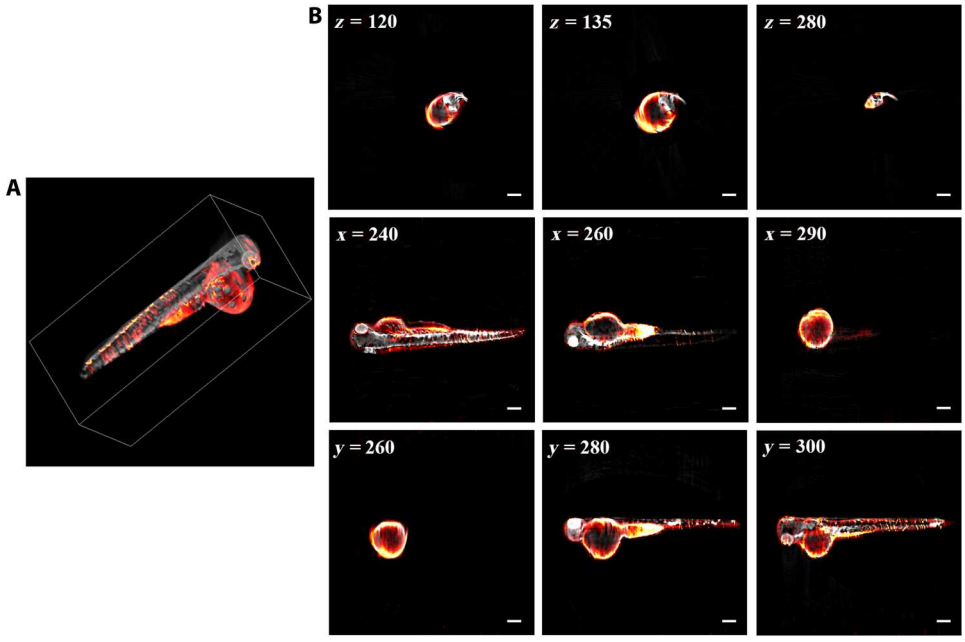

Fig. 3. Volumetric imaging of zebrafish by the ORPT system. (**A**) The 3D fusion image of zebrafish. (**B**) The selected section images (in transverse, sagittal, and coronal views) from the reconstructed images. Scale bars, 200 μm.

corresponding reconstructed 3D results can be seen in movies S10 to S12 and fig. S6.

Visualizing the fat body of *D. melanogaster* at different developmental stages in 3D

D. melanogaster is an important model organism with the characteristics of short life cycle, cost-effectiveness, and ease of manipulation. It has been used in a wide range of applications in genetics and developmental biology, such as carbohydrate, sterol, and lipid metabolism (*43*, *44*). Because of its homology in many enzymes and metabolic pathways with human, most of the *D. melanogaster* research is commonly focused on the basic metabolism functions and disease-related genes in humans (*45*). Lipid droplets act as a fat repository in cells and tissue, facilitating homeostasis and lipid metabolism. Furthermore, it stores thousands of different proteins, which can be used to study the trafficking dynamics and biological significance (*46*). The *D. melanogaster* fat body (one of an organ) stores lipid to feed the animal during its larval stage and performs lipid metabolism and hormone production (*45*); thus, it is crucial to study it at different developmental stages.

To this end, we explored the 3D microstructure and chemical components of the *D. melanogaster* fat body using our ORPT system at different stages (first, second, and third instar larva) within the range of 2457 to 3123 cm^{-1} vibrational window. We obtained the optical projection images of the *D. melanogaster* fat body (fig. S7A). Raman images of the fat body at different developmental stages were observed along with the use of the Raman channel, as shown in fig. S7B, which yielded the lipid and protein information of the fat body and microstructural information of internal organs, including the gut, trachea, and fat body. Besides, we observed the change in the fat body during the development, and the corresponding reconstructed results are described in fig. S7.

Figure 5A shows the volumetric reconstruction image of first-instar larva of *D. melanogaster* in a volume of ~1.66 mm by 1.66 mm by 1.66 mm and the selected slice images of the reconstructed results. We could infer that the morphology and chemical distribution of the larva can be well reconstructed, with the fat body attached to the salivary gland with high Raman signal. Similarly, the Raman signal, which represents the distribution of lipid or protein, agreed well with the corresponding location of the *D. melanogaster* structure with little distortion, as can be seen from the selected images in different directions (Fig. 5, B to D). Furthermore, we chose a second instar larva to explore the change in the fat body. A 3D fused reconstruction image is shown in Fig. 5F, where the internal organs, such as the gut and fat body as well as the lipid or protein distribution of the fat body in a volume of ~2.66 mm by 2.66 mm by 2.66 mm can be seen. Meanwhile, we obtained the sectioning images by selecting different planes along the transverse, sagittal, and coronal planes, as shown in Fig. 5 (G to I), with a magnification of the lens of ×5. We resolved the fat body or the fat tissue from the Raman image (pseudo-colored in red), and resolved the microstructure information from the OPT signal. The abovementioned results revealed that the internal organs have started developing at this stage, and compared with the first instar larva, the fat body was reduced because it was feeding the body during the growth stage. The detailed images of the fat body changes at different developmental stages can be found in fig. S7B.

Last, we investigated the microstructure and chemical distribution information of the third instar larva of *D. melanogaster* in a volume of ~4.43 mm by 4.43 mm by 4.43 mm, as shown in Fig. 5K. We observed the fat body around the trachea at the posterior end from the volumetric information. By carefully examining the larva, we observed many lipids to be distributed around the salivary gland and tail (Fig. 5, L to N). Thus, we confirmed the fat body to be transformed from an organized tissue to individual fat cells or

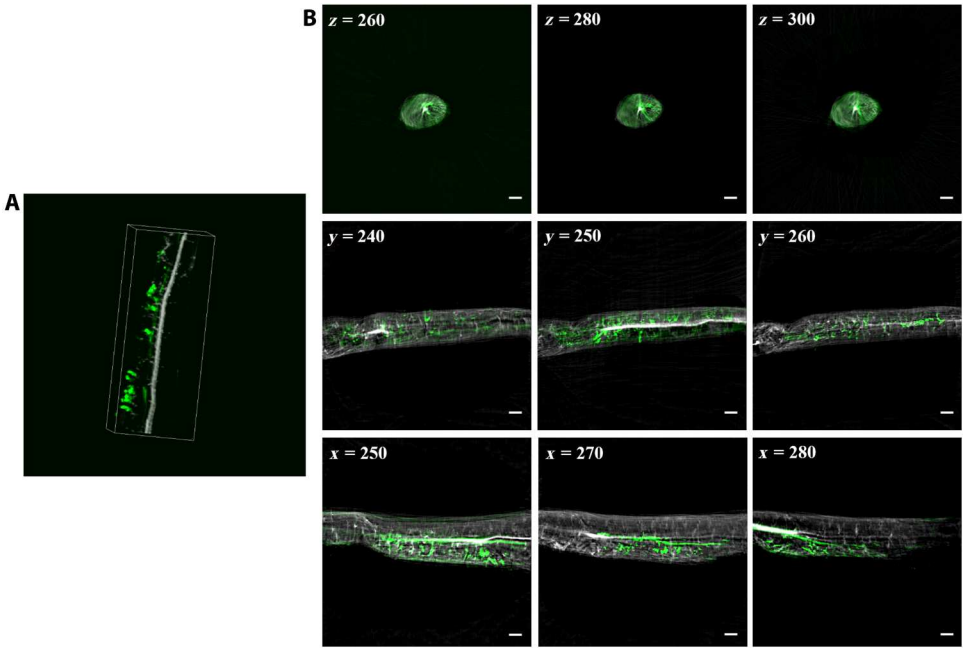

Fig. 4. Volumetric imaging results of the *Arabidopsis* stem. (**A**) Reconstruction images fused by the volumetric Raman and optical images. (**B**) Sectional images at different views, acquired by the reconstructed results of Raman and OPT. Scale bars, 100 μm.

others during the developmental stage. Following literature (*45*), we found that the fat body at this late stage would remodel itself. The Raman projection images showed these changes of the fat at different developmental stages, as shown in Fig. 5 (E, J, and O). However, because the larva in these experiments was not transparentized and the spatial resolution of the system was limited, the 3D reconstructed image did not show finer microstructural information. All the reconstruction results at different developmental stages can be seen in fig. S7 (C and D). As for the dual-modality projection images and 3D fusion images of *D. melanogaster* at different development stages, they can be found in movies S13 to S21.

The analyses of these data demonstrate that our ORPT system can easily detect the microstructural and molecular information of a biological system. Moreover, this can facilitate the studies of in vivo, fast imaging, and accurate quantification of 3D samples in a label-free manner.

DISCUSSION

In this work, we demonstrated the ORPT for label-free microstructural and molecular volumetric imaging of millimeter-scale samples. Our findings showed that our ORPT system can resolve the 3D distribution of molecules and structural information in a volume with micron-level spatial resolution from the same device. First, we verified the feasibility of our proposed ORPT system and the probability of the FBP algorithm for 3D reconstruction by detecting the single and multiple PS beads in a volume. Next, we demonstrated the applicability of our proposed methodology by volumetric fusion imaging of zebrafish and *A. thaliana* in a volume, separately. The results concluded that this technique can be used for the visualization of the microstructural and molecular information of biological samples. Last, we showed that the proposed ORPT system can be used as an imaging tool to monitor the lipid and protein metabolism process in *D. melanogaster*. To identify the morphology of lipid and protein distribution during different developmental stages, we recorded the fat body changes of *D. melanogaster* at the microstructure level followed by Raman imaging. These related fusion results revealed that this technique can facilitate the development of in vivo imaging and can be used as a quantitative imaging tool for accurate quantification.

This work has some limitation, and there is plenty of room for further improvement of our ORPT system. First, the spectral resolution can be further improved. We used a filter wheel with six filters for the detection of Raman signals at different wave numbers due to the limitation of the field depth of the lens, which induced the collected Raman signal as a mixed spectral image. To achieve accurate analysis of the composition information of a substance at a certain characteristic peak, two aspects can be improved. On the one hand, to accurately detect the molecule information within the imaging field depth, the filter wheel should be replaced with a small and high-precision tunable filter. On the other hand, the resulting images can be appropriately separated at a characteristic band using a deep learning network (*47*). Second, the SNR and imaging speed can be improved. Here, to reduce the damage of the sample caused by the laser, we fivefold expanded the laser beam, where the density of the laser power was around 0.8 mW/mm^2. Thus, we obtained a high-quality Raman image by increasing the integration time up to 8 s. However, a longer time is limiting for rapid, in vivo imaging of biological samples, and it is difficult to monitor the fast-imaging process. It has already been reported (*48*, *49*) that the damage thresholds of biological samples can reach several tens of watts per square centimeters under the excitation wavelength of 532 nm, which is much higher than that in our experimental setups. Thus, we can further reduce the integration time and properly increase the laser power for higher SNR Raman images of 3D reconstruction. Third, the processing and

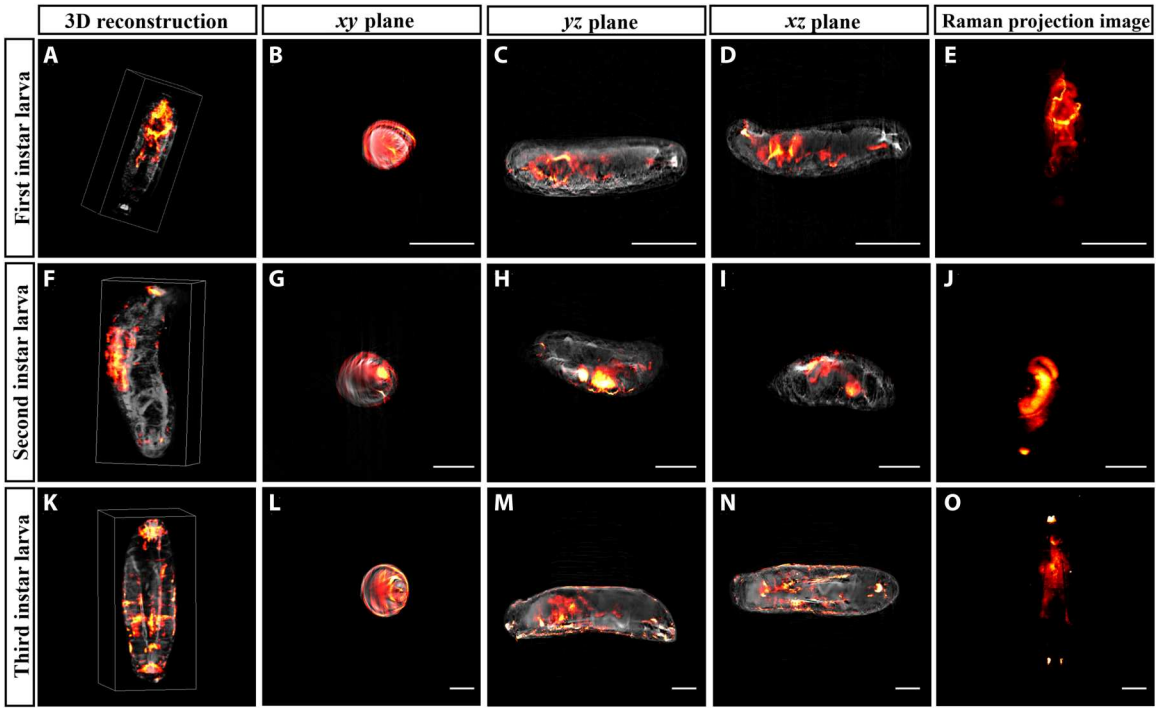

Fig. 5. The fat body imaging of *D. melanogaster* at different developmental stages. (**A**, **F**, and **K**) The 3D reconstructed image. (**B** to **D**, **G** to **I**, and **L** to **N**) Sectional images along different planes in the first-, second-, and third-instar larvae of *D. melanogaster*, respectively. (**E**, **J**, and **O**) Raman projection image of the fat body at different developmental stages. Scale bars, 500 μm.

fixation of the sample can be further improved. Now, we directly fixed the sample with low-melting agarose gel in a capillary, and then, we collected the projection images of the capillary. However, the effects of light scattering from the opacity of the sample were very detrimental to the 3D visualization. This can be overcome by exploring efficient and nondestructive optical clearing reagents (*50*, *51*) that can enhance the transparency of the sample while maintaining the Raman scattering signal generation capability. On the other hand, the existing sample fixation method is not conducive to keeping samples in a viable state for long periods of time. Thus, a complementary sample fixation module can be designed, such as petri dish fixation method (*11*), which can reduce the damage to the specimen and be more conducive to longitudinal observation for in vivo imaging. Last, in the current stage, the Raman projection imaging module focuses only on the high–wave number C-H region. This is mainly considered for two reasons. The first one is that the characteristic peaks of lipids and proteins fall mainly in this region, and these two types of components are very important in biology and medicine (*32*, *52*). The second one is the strong Raman signal in this region, which is advantageous in verifying the feasibility and exploring the application potential of our ORPT technique. Through some technical optimization, including increasing the laser power, improving the Raman signal collection efficiency, and replacing suitable filters, our ORPT system is also capable of collecting Raman signals from other wave number regions, such as fingerprint features.

Our ORPT technology is based on projection tomography framework. ORPT inherits the advantages and disadvantages of projection tomography in addition to the features of label-free microstructure and molecular component visualization. Projection tomography is a volumetric imaging technique that incorporates sample rotation, image projection, and tomographic reconstruction strategies and has the superiority of providing high isotropic spatial resolution, rapid 3D imaging of living samples at the microscopic to mesoscopic scale. Likewise, our ORPT technique faces problems associated with projection tomography. For example, samples require special fixation for effective rotation and long-term activity, traditional FBP reconstruction brings a high number of projection images and excessive light dose, and dual-modality imaging can only be performed on transparent or weakly scattering biological samples. These can be addressed by designing complementary sample processing and fixation module and developing advanced reconstruction algorithms, which represent further work in progress.

MATERIALS AND METHODS

Performance of the ORPT system

In the current setup, we determined the imaging field of view by the depth of field of the lens. The magnification of the lens determines the depth of field and the spatial resolution of the system. The larger the magnification, the smaller the depth of field of the system and the higher the spatial resolution; conversely, the larger the depth of field of the system, the lower the spatial resolution. With the current setup, the range of sample sizes (x, y, and z) determined by the depth of field of the system can be measured between 1.48 mm by 1.48 mm by 1.48 mm and 9.5 mm by 9.5 mm by 9.5 mm.

We prepared various concentrated solutions of DMSO in D_2O (8.4, 5.6, 4.2, 2.8, 2.52, 2.24, 1.97, 1.41 1.12, 0.28, and 0.07 M) to detect the sensitivity of the Raman signal, obtained by the ORPT

system. We stored the solution in a quartz cuvette. To excite the DMSO Raman signal at 2457 to 3123 cm^{-1}, the laser-powered density of the sample was set to 0.87 mW/mm^2, while the integration time was set to 10 s for all measurements. To investigate the relationship between the laser power and Raman signal intensity, the power of the laser was set to 215.4, 208.5, 152.1, 74.4, 60.7, 43.4, and 26.1 mW, separately.

Feasibility verification of the ORPT system

To capture the images of PS beads, we tuned the central wavelength of the filter in the detection path to 625 nm using a filter wheel, corresponding to 2457 to 3123 cm^{-1}, and detected the dual-modality signals of the sample in this vibrational window. We set the laser power density of the sample to 0.87 mW/mm^2 and adjusted the faced light intensity to the optimal contrast of the imaging sample. We fixed the capillary onto the rotational stage and consecutively rotated at 180° with 1° per step. Then, we collected the projected images and assembled them using the FBP algorithm to reconstruct the microstructure and chemical composition information within a volume of 1.48 mm by 1.48 mm by 1.48 mm, as shown in fig. S2 (A, C, D, and F).

Sample preparation

DMSO was purchased from Tianjin Tianli Chemical Reagent Co. Ltd. The involved PS beads were purchased from Shanghai ZzBio Co. Ltd. The transparent zebrafish were purchased from Shanghai GeneBio Co. Ltd. The *D. melanogaster* at different development stages was obtained from the Shaanxi Normal University.

PS beads imaging

We performed the ORPT system imaging of single and multiple PS beads of 100 μm (ZPH-134, PHOSPHOREX, USA), respectively. We first suspended the beads in a 1% cured low-melting agarose gel and then transferred them into a capillary to prevent particle movement during the projection image acquisition. We set the integral time to 0.1 s for each projection image in the light path and to 8 s in the Raman path. We imaged the PS beads in a volume of ~1.48 mm by 1.48 mm by 1.48 mm. The total acquisition time for optical projection images was 18 s, while that for the Raman was 1440 s.

Biological sample imaging

The transparent zebrafish were kept transparent in 1-phenyl-2-thiourea, reared, and maintained according to the standard practices at 28°C. We prepared the sample using a similar way as the beads. We collected the dual-modality projection images of 180 at an angle increment of 1° with 0.1- and 8-s integral time, respectively. Each projected image was of 1024 × 1024 pixels. We obtained the sectional images from the corresponding reconstructed results of optical and Raman channels. We magnified the zebrafish to ×3, corresponding to 16.97 μm of spatial resolution. The laser power density of the sample was about 0.76 mW/mm^2.

As for the ORPT system imaging of the *A. thaliana* stem, we chose the wild-type seeds of the Columbia-0 ecotype to germinate on MS plates and then transplanted the soil matrix after a week. We selected the stem of a 3-week-old *Arabidopsis* for imaging. First, we fixed the selected stem in the FAA solution (formalin:glacial acetic acid:70% ethanol, 1:1:18). Then, we dehydrated the stem in 70, 95, 100, and 100% ethanol solutions, separately. The concentration gradient treatment time was 30 min for each solution, and we then placed them in a refrigerator at 4°C overnight. On the subsequent day, we placed the imaging stem in 95, 70, 50, 30, and 15% ethanol solution for rehydration for 30 min, separately, and then placed them in a clearing reagent (chloral hydrate:glycerol:water, 8:1:2) for transparency. Last, we used a dropper to take out the transparent stem for imaging. The sample preparation was similar to that of zebrafish.

The *D. melanogaster* at a different developmental stage was raised at 25°C using an agar diet (sugar, 81.5 g/liter; yeast powder, 9.2 g/liter; sodium benzoate, 1.3 g/liter; corn flour, 108.5 g/liter; agar, 8.2 g/liter). Before observation, we stunned the larva with ether and then transferred it to 1% low-melting agarose for fixation.

Image processing and reconstruction

In our experiments, the collected multiangle projection images need to be preprocessed before 3D reconstruction, including the bright-field and dark-field corrections. The dark-field correction is to remove the background noise of the camera, and the bright-field correction is to reduce the inhomogeneity of the light source. First, we collected multiple dark-field and bright-field images. Second, we calculated the mean matrices of these images. In the end, we performed the dark- and bright-field corrections. We performed the dark-field correction by subtracting the mean matrix of the dark-field images from the projection image, which enhances the contrast of the projection image. The bright-field correction is slightly complicated and can be performed according to the following steps: (i) A difference matrix is obtained by subtracting the mean matrix of the dark-field image from the mean matrix of the bright-field image; (ii) an intermediate matrix is obtained by point dividing this difference matrix by the dark-field corrected projection image; and (iii) the mean value of the difference matrix is calculated and multiplied by the previous intermediate matrix. These operations can correct the shadows of the acquired projection images. We acquired 50 bright-field images and 50 dark-field projection images, respectively.

We processed the projected images using the ImageJ software. We wrote the 3D reconstruction of dual-modality data using the FBP algorithm in MATLAB (MathWorks Inc.). We achieved the visualization and analysis of the volumetric images using the ImageJ software and the 3D fusion videos of different samples using a 3D slicer software.

Supplementary Materials

This PDF file includes:
Supplementary Text
Figs. S1 to S7
Legends for movies S1 to S21

Other Supplementary Material for this manuscript includes the following:
Movies S1 to S21

View/request a protocol for this paper from *Bio-protocol*.

REFERENCES AND NOTES

1. J. C. M. Gebhardt, D. M. Suter, R. Roy, Z. Q. W. Zhao, A. R. Chapman, S. Basu, T. Maniatis, X. S. Xie, Single-molecule imaging of transcription factor binding to DNA in live mammalian cells. *Nat. Methods* **10**, 421–426 (2013).

2. J. Sharpe, U. Ahlgren, P. Perry, B. Hill, A. Ross, J. Heckshenr-Sorensen, R. Baldock, D. Davidson, Optical projection tomography as a tool for 3D microscopy and gene expression studies. *Science* **296**, 541–545 (2002).
3. E. A. Susaki, C. Shimizu, A. Kuno, K. Tainaka, X. Li, K. Nishi, K. Morishima, H. Ono, K. L. Ode, Y. Saeki, K. Miyamichi, K. Isa, C. Yokoyama, H. Kitaura, M. Ikemura, T. Ushiku, Y. Shimizu, T. Saito, T. C. Saido, M. Fukayama, H. Onoe, K. Touhara, T. Isa, A. Kakita, M. Shibayama, H. R. Ueda, Versatile whole-organ/body staining and imaging based on electrolyte-gel properties of biological tissues. *Nat. Commun.* **11**, 1982 (2020).
4. C. Y. Fang, T. T. Yu, T. T. Chu, W. Y. Feng, F. Zhao, X. C. Wang, Y. J. Huang, Y. S. Li, P. Wan, W. Mei, D. Zhu, P. Fei, Minutes-timescale 3D isotropic imaging of entire organs at subcellular resolution by content-aware compressed-sensing light-sheet microscopy. *Nat. Commun.* **12**, 107 (2021).
5. Q. Y. Zhong, A. A. Li, R. Jin, D. J. Zhang, X. N. Li, X. Y. Jia, Z. H. Ding, P. Luo, C. Zhou, C. Y. Jiang, Z. Feng, Z. H. Zhang, H. Gong, J. Yuan, Q. M. Luo, High-definition imaging using line-illumination modulation microscopy. *Nat. Methods* **18**, 309–315 (2021).
6. B. J. Chang, J. D. Manton, E. Sapoznik, T. Pohlkamp, T. S. Terrones, E. S. Welf, V. S. Murali, P. Roudot, K. Hake, L. Whitehead, A. G. York, K. M. Dean, R. Fiolka, Real-time multi-angle projection imaging of biological dynamics. *Nat. Methods* **18**, 829–834 (2021).
7. J. Sharpe, Optical projection tomography as a new tool for studying embryo anatomy. *J. Anat.* **202**, 175–181 (2003).
8. B. Yang, M. Lange, A. Millett-Sikking, X. Zhao, J. Bragantini, S. Vijaykumar, M. Kamb, R. Gomez-Sjoberg, A. C. Solak, W. P. Wang, H. Kobayashi, M. N. McCarroll, L. W. Whitehead, R. P. Fiolka, T. B. Kornberg, A. G. York, L. A. Royer, Daxi-high-resolution, large imaging volume and multi-view single-objective light-sheet microscopy. *Nat. Methods* **19**, 461–469 (2022).
9. L. Slivestri, M. C. Mullenbroich, I. Costantini, A. P. Di Giovanna, G. Mazzamuto, A. Franceschini, D. Kutra, A. Kreshuk, C. Checcucci, L. O. Toresano, Universal autofocus for quantitative volumetric microscopy of whole mouse brains. *Nat. Methods* **18**, 953–958 (2021).
10. T. Bruns, S. Schickinger, H. Schneckenburger, Sample holder for axial rotation of specimens in 3D microscopy. *J. Microsc.* **260**, 30–36 (2015).
11. N. Wang, D. F. Chen, D. Chen, C. P. Bao, J. M. Liang, X. L. Chen, S. P. Zhu, Feasibility study of limited-angle reconstruction for in vivo optical projection tomography based on novel sample fixation. *IEEE Access* **7**, 87681–87691 (2019).
12. S. Fukumoto, T. Fujimoto, Deformation of lipid droplets in fixed samples. *Histochem. Cell Biol.* **118**, 423–428 (2002).
13. M. J. Boot, C. H. Westerberg, J. Sanz-Ezquerro, J. Cotterell, R. Schweitzer, M. Torres, J. Sharpe, In vitro whole-organ imaging: 4D quantification of growing mouse limb buds. *Nat. Methods* **5**, 609–612 (2008).
14. C. Pardo-Martin, A. Allalou, J. Medina, P. M. Eimon, C. Wahlby, M. F. Yanik, High-throughput hyperdimensional vertebrate phenotyping. *Nat. Commun.* **4**, 1467 (2013).
15. J. X. Cheng, X. S. Xie, Vibrational spectroscopic imaging of living systems: An emerging platform for biology and medicine. *Science* **350**, eaaa8870 (2015).
16. K. Yen, T. T. Le, A. Bansal, D. Narasimhan, J. X. Cheng, H. A. Tissenbaum, A comparative study of fat storage quantitation in nematode caenorhabditis elegans using label and label-free methods. *PLOS ONE* **5**, e12810 (2010).
17. C. Krafft, I. W. Schie, T. Meyer, M. Schmitt, J. Popp, Developments in spontaneous and coherent Raman scattering microscopic imaging for biomedical applications. *Chem. Soc. Rev.* **45**, 1819–1849 (2016).
18. R. Hellwart, P. Christen, Nonlinear optical microscopic examination of structure in polycrystalline ZnSe. *Opt. Commun.* **12**, 318–322 (1974).
19. E. Nitiss, J. Q. Hu, A. Stroganov, C. S. Bres, Optically reconfigurable quasi-phase-matching in silicon nitride microresonators. *Nat. Photonics.* **16**, 134–141 (2022).
20. D. Debarre, W. Supatto, A. M. Pena, A. Fabre, T. Tordjmann, L. Combettes, M. C. Schanne-Klein, E. Beaurepaire, Imaging lipid bodies in cells and tissues using third-harmonic generation microscopy. *Nat. Methods* **3**, 47–53 (2006).
21. M. S. Pochechuev, A. A. Lanin, I. V. Kelmanson, A. S. Chebotarev, E. S. Fetisova, D. S. Bilan, E. K. Shevchenko, A. A. Ivanov, A. B. Fedotov, V. V. Belousov, A. M. Zheltikov, Multimodal nonlinear-optical imaging of nucleoli. *Opt. Lett.* **46**, 3608–3611 (2021).
22. M. Abu Bakkar, H. Nawaz, M. I. Majeed, A. Naseem, A. Ditta, N. Rashid, S. Ali, J. Bajwa, S. Bashir, S. Ahmad, H. Hyat, K. S. Bukhari, F. Bonnier, Raman spectroscopy for the qualitative and quantitative analysis of solid dosage forms of Sitagliptin. *Spectrochim. Acta A Mol. Biomol. Spectrosc.* **245**, 118900 (2021).
23. N. Wang, H. Cao, L. Wang, F. Ren, Q. Zeng, X. Y. Xu, J. M. Liang, Y. H. Zhan, X. L. Chen, Recent advances in spontaneous Raman spectroscopic imaging: Instrumentation and applications. *Curr. Med. Chem.* **27**, 6188–6207 (2020).
24. C. H. Camp, M. T. Cicerone, Chemically sensitive bioimaging with coherent Raman scattering. *Nat. Photonics* **9**, 295–305 (2015).
25. Y. Oshima, H. Sato, H. Kajiura-Kobayashi, T. Kimura, K. Naruse, S. Nonaka, Light sheet-excited spontaneous Raman imaging of a living fish by optical sectioning in a wide field Raman microscope. *Opt. Express* **20**, 16195–16204 (2012).
26. X. L. Chen, C. Zhang, P. Lin, K. C. Huang, J. M. Liang, J. Tian, J. X. Cheng, Volumetric chemical imaging by stimulated Raman projection microscopy and tomography. *Nat. Commun.* **8**, 15117 (2017).
27. N. Wang, X. Y. Wang, F. Ren, T. Y. Yan, H. Xie, S. P. Zhu, X. L. Chen, Feasibility study of dual-modality optical-Raman projection tomography. *Proc. SPIE* , 1197304 (2022).
28. X. M. Zhang, S. Y. Wang, Y. B. Shi, H. Yuan, Z. M. Ma, F. Wang, Z. D. Lin, L. Qin, J. Liu, Quantitative analysis of spectral characteristics and concentration of ensembles of NV^- centers in diamond. *Diamond Relat. Mater.* **76**, 21–26 (2017).
29. K. Howe, M. D. Clark, C. F. Torroja, J. Torrance, C. Berthelot, M. Muffato, J. E. Collins, S. Humphray, K. McLaren, L. Matthews, The zebrafish reference genome sequence and its relationship to the human genome. *Nature* **496**, 498–503 (2013).
30. M. Andreana, C. Sturtzel, C. P. Spielvogel, L. Papp, R. Leitgeb, W. Drexler, M. Distel, A. Unterhuber, Toward quantitative in vivo label-free tracking of lipid distribution in a zebrafish cancer model. *Front. Cell Dev. Biol.* **9**, 746196 (2021).
31. H. Hogset, C. C. Horgan, J. P. K. Armstrong, M. S. Bergholt, V. Torraca, Q. Chen, T. J. Keane, L. Bugeon, M. J. Dallman, S. Mostowy, M. M. Stevens, In vivo biomolecular imaging of zebrafish embryos using confocal Raman spectroscopy. *Nat. Commun.* **11**, 6172 (2020).
32. Z. L. Yu, T. Chen, X. N. Zhang, D. Fu, X. Liao, J. Shen, X. X. Liu, B. Zhang, X. S. Xie, X. D. Su, J. Y. Chen, Y. Y. Huang, Label-free chemical imaging in vivo: Three-dimensional non-invasive microscopic observation of amphioxus notochord through stimulated Raman scattering (SRS). *Chem. Sci.* **3**, 2646–2654 (2012).
33. A. Akiva, G. Malkinson, A. Masic, M. Kerschnitzki, M. Bennet, P. Fratzl, L. Addadi, S. Weiner, K. Yaniv, On the pathway of mineral deposition in larval zebrafish caudal fin bone. *Bone* **75**, 192–200 (2015).
34. M. Bennet, A. Akiva, D. Faivre, G. Malkinson, K. Yaniv, S. Abdelilah-Seyfried, P. Fratal, A. Masic, Simultaneous Raman microspectroscopy and fluorescence imaging of bone mineralization in living zebrafish larvae. *Biophys. J.* **106**, L17–L19 (2014).
35. W. Muller, M. Kielhorn, M. Schmitt, J. Popp, R. Heintzmann, Light sheet Raman microspectroscopy. *Optica* **3**, 452–457 (2016).
36. M. Schmidt, A. M. Schwartzberg, A. Carroll, A. Chaibang, P. D. Adams, P. J. Schuck, Raman imaging of cell wall polymers in Arabidopsis thaliana. *Biochem. Biophys. Res. Commun.* **395**, 521–523 (2010).
37. B. P. Mateu, M. T. Hauser, A. Heredia, N. Gierlinger, Waterproofing in Arabidopsis: Following phenolics and lipids in situ by confocal Raman microscopy. *Front. Chem.* **4**, 10 (2016).
38. F. Beisson, Y. Li-Beisson, M. Pollard, Solving the puzzles of cutin and suberin polymer biosynthesis. *Curr. Opin. Plant Biol.* **15**, 329–337 (2012).
39. M. A. Atmodjo, Z. Y. Hao, D. Mohnen, Evolving views of pectin biosynthesis. *Ann. Rev. Plant Biol.* **64**, 747–779 (2013).
40. O. Piot, J. Autran, M. Manfait, Investigation by confocal Raman microspectroscopy of the molecular factors responsible for grain cohesion in *Thetriticum aestivum* bread wheat. Role of the cell walls in the starchy endosperm. *J. Cereal Sci.* **34**, 191–205 (2001).
41. H. E. McFarlane, A. Döring, S. Persson, The cell biology of cellulose synthesis. *Ann. Rev. Plant Biol.* **65**, 69–94 (2014).
42. J. Barros, H. Serk, I. Granlund, E. Resquet, The cell biology of lignification in higher plants. *Ann. Bot.* **115**, 1053–1074 (2015).
43. K. D. Baker, C. S. Thummel, Diabetic larvae and obese flies emerging studies of metabolism in Drosophila. *Cell Metab.* **6**, 257–266 (2007).
44. K. N. Bharucha, The epicurean fly: Using Drosophila melanogaster to study metabolism. *Pediatr. Res.* **65**, 132–137 (2009).
45. C. H. Chien, W. W. Chen, J. T. Wu, T. C. Chang, Label-free imaging of Drosophila in vivo by coherent anti-Stokes Raman scattering and two-photon excitation autofluorescence microscopy. *J. Biomed. Opt.* **16**, 016012 (2011).
46. W. Dou, D. L. Zhang, Y. Jung, J. X. Cheng, D. M. Umulis, Label-free imaging of lipid-droplet intracellular motion in early drosophila embryos using femtosecond-stimulated Raman loss microscopy. *Biophys. J.* **102**, 1666–1675 (2012).
47. Y. F. Xu, S. G. Deng, X. L. Li, Y. He, A sparse unmixing model based on NMF and its application in Raman image. *Neurocomputing* **207**, 120–130 (2016).
48. M. L. Denton, M. S. Foltz, K. J. Schuster, L. E. Estlack, R. J. Thomas, Damage thresholds for cultured retinal pigment epithelial cells exposed to lasers at 532 nm and 458 nm. *J. Biomed. Opt.* **12**, 034030 (2007).
49. H. J. Foth, S. Farber, A. Gauer, R. Wagner, Thermal damage threshold at 633 nm of tympanic membrane of pig. *Hear. Res.* **142**, 71–78 (2000).
50. J. J. Li, P. Lin, Y. Y. Tan, J. X. Cheng, Volumetric stimulated Raman scattering imaging of cleared tissues towards three-dimensional chemical histopathology. *Biomed. Opt. Express* **10**, 4329–4339 (2020).

51. M. Wei, L. Y. Shi, Y. H. Shen, Z. L. Zhao, A. Guzman, L. J. Kaufman, L. Wei, W. Min, Volumetric chemical imaging by clearing-enhanced stimulated Raman scattering microscopy. *Proc. Natl. Acad. Sci. U.S.A.* **116**, 6608–6617 (2019).
52. J. H. Lee, D. H. Kim, W. K. Song, M. K. Oh, D. K. Ko, Label-free imaging and quantitative chemical analysis of Alzheimer's disease brain samples with multimodal multiphoton nonlinear optical microspectroscopy. *J. Biomed. Opt.* **20**, 056013 (2015).

Acknowledgments: We thank J.-X. Cheng at Boston University for helpful discussions. We are grateful to EditSprings (www.editsprings.cn) for the expert linguistic services provided. **Funding:** This work was supported by the National Natural Science Foundation of China, grants 81871397, 81627807, and 62275210 (X.C.); the National Young Talent Program (X.C.); the Shaanxi Science Fund for Distinguished Young Scholars, grant 2020JC-27 (X.C.); the Key Research and Development Program of Shaanxi, grant 2021ZDLSF04-05 (Q.Z.); the Shaanxi Young Top-notch Talent Program; the Fundamental Research Funds for Central Universities, grants QTZX2185 (Q.Z.) and QTZX22065 (D.Z.); and the National Key R&D Program of China, grant 2018YFC0910600 (X.C.). **Author contributions:** Conceptualization: N.W. and X.C. Methodology: N.W., X.W., T.Y., X.C., and S.Z. Investigation: N.W., L.W., F.R., H.X., and D.C. Visualization: N.W., L.W., D.Z., and Q.Z. Supervision: X.C. and S.Z. Writing—original draft: N.W., X.C., and H.X. Writing—review and editing: N.W., X.C., S.Z., and H.X. **Competing interests:** X.C., N.W., and S.Z. are inventors on an awarded patent (U.S. 10,365,219 B1; date of patent: 30 July 2019) held by Xidian University that covers the dual-modality ORPT system. All other authors declare that they have no competing interests. **Data and materials availability:** All data needed to evaluate the conclusions in the paper are present in the paper and/or the Supplementary Materials. Original data acquired by the developed ORPT system and code for image processing and reconstruction are available at https://zenodo.org/record/7669963#.Y_hNYCZByUk.

Submitted 15 October 2022
Accepted 24 February 2023
Published 24 March 2023
10.1126/sciadv.adf3504